May 2024

PREDICTABILITY OF THE OVERLAND REINTENSIFICATION OF NORTH ATLANTIC TROPICAL CYCLONE ERIN (2007)

Ariel Tickner-Ernst
University of Wisconsin-Milwaukee

PREDICTABILITY OF THE OVERLAND REINTENSIFICATION OF NORTH ATLANTIC TROPICAL CYCLONE ERIN (2007)

by

Ari Tickner-Ernst

A Thesis Submitted in

Partial Fulfillment of the

Requirements for the Degree of

Master of Science

in Atmospheric Science

at

The University of Wisconsin-Milwaukee

May 2024

ABSTRACT

PREDICTABILITY OF THE OVERLAND REINTENSIFICATION OF NORTH ATLANTIC TROPICAL CYCLONE ERIN (2007)

by

Ari Tickner

The University of Wisconsin-Milwaukee, 2024
Under the Supervision of Professor Clark Evans

Tropical cyclones (TC) typically decrease in intensity upon interacting with land because of increased surface roughness and decreased surface evaporation. However, several studies have documented cases in which TCs maintain their intensity or even intensify over land within non- or weakly baroclinic environments. Yet, our understanding of the precise physical processes that support maintenance or intensification over land in non- or weakly baroclinic environments remains limited, and the predictive skill for these outcomes has yet to be quantified.

We begin this process by quantifying the predictive skill and forecast uncertainty of the overland intensification of North Atlantic Tropical Storm Erin in 2007 using a 50-member ensemble of free forecasts initialized from the output of an ensemble adjustment Kalman Filter-based cycled data assimilation system using the Data Assimilation Research Testbed software and Advanced Research Weather Research and Forecasting model. The ensemble outputs are then analyzed using ensemble sensitivity analysis (to provide meaningful physical insight into the relevant forecast sensitivities, even in environments where non-linear processes are important), ensemble subsetting (e.g., strong versus weak TCs), and others, to assess the sensitivity in overland intensity to finite-amplitude atmospheric variability. Additionally, simpler measures such as intensity variability across the ensemble are utilized as part of the analysis, which we compare to both over-water intensification cases and idealized simulations of overland intensity change.

We then take different surface and vertical level observation types plot them for both the prior and posterior analyses to compare the observation diagnostics at each analysis time. Optimal performance is achieved when the RMSE and spread are close in magnitude to each other, which could be indicative of well-tuned observation error statistics (Romine et al. 2013). Along with the evaluation of different observation diagnostics, a comprehensive analysis of ensemble outputs is conducted (Figs. 13, 14). Members are categorized into GOOD and BAD members, to help delineate which members best represent Erin's intensity late on 18 August and the early hours of 19 August 2007 (Figs. 15, 16), which are determined with the help of MSLP, where the good members display at least one closed isobar for an extended period of time in the simulation, and bad members experience near-immediate dissipation.

TABLE OF CONTENTS

LIST OF FIGURES

LIST OF TABLES

ACKNOWLEDGEMENTS

First and foremost, I would like to thank my advisor Dr. Clark Evans for all of his help and advising throughout this project while allowing me to continue my career path in atmospheric sciences at the University of Wisconsin-Milwaukee. This has been an invaluable opportunity that I will never forget and am grateful to have had.

Also, a special thank you to Drs. Paul Roebber and Sergey Kravtsov for serving on my thesis committee.

Lastly, I want to shout out all the friends, classmates, and family that have made this project all possible. It has been a long journey and you have always been there to provide support, and I will always be thankful for that.

1. Introduction

Tropical cyclones (TCs) generally (given the right conditions, ranging from ocean waters of at least 26.5°C throughout a sufficient depth, to a pre-existing near-surface disturbance with sufficient vorticity and convergence, a relatively moist mid-troposphere, and more; Landsea 2000) strengthen over open oceans, as the waters are one of their primary energy sources for intensification. Typically, TCs lose their intensity upon landfall, due to increased surface roughness (a measure of given land-surface protrusions, where areas with greater surface roughness display more protruding characteristics) and decreased surface evaporation (Tuleya 1994, Shen et al. 2002). Increased surface roughness also disproportionately affects the intensity throughout the TC, with a much more accelerated decline of the intense winds near the storm's center (Chen and Chavas 2020, Hlywiak and Nolan 2021). However, recent studies (e.g., Shen et al. 2002, Emanuel et al. 2008, Evans et al. 2011, Chen and Chavas 2020, and Hlywiak and Nolan 2021) have suggested that there may be instances in which a TC can intensify, or its weakening is suppressed, after landfall, in non- and weakly baroclinic environments. Notable examples of such types of TC's include Erin (2007; Monteverdi and Edwards 2010; Evans et al. 2011; Kellner et al. 2011), Abigail (2001; Emanuel et al. 2008), and Kelvin (2018; Yoo et al. 2020). A better understanding of the characteristics that lead to TC maintenance or intensification will be beneficial in producing more reliable forecasts going forward, over both water and land.

Water depth over land may play a role in the decreased suppression of TC intensity. There is a correlation between water depth and intensity of TCs, where larger water depths typically spell a slower decrease in intensity, as it lags behind the largest surface cooling (Fig. 1; Shen et al. 2002). For example, a 200-cm water layer will better retain the intensity of a TC once it crosses land compared to a shallow water or water-barren surface, as the impact of the surface flux and evaporation reduction is smaller in this case (Shen et al. 2002). However, there are more

noticeable diurnal variations/patterns at more shallow water depths (i.e., more fluctuations in TC intensity), because the temperature of the subsurface layer (which has a small heat capacity) is quite sensitive to the diurnal cycle of solar radiation. For example, a 50-cm water depth may experience relatively large diurnal variations, with greater intensity during the day and weaker intensity at night, as compared to a 200-cm depth, where the solar radiation may take longer to travel to, and the intensity is more constant as a result (Shen et al. 2002). Specifically, with a half-meter surface water layer, the amplitude of the diurnal variation of the central pressure is approximately 7 mb, and roughly 5 m s^{-1} for the maximum surface wind (Shen et al. 2002). The surfaces with smaller water depths also display a more rapid increase in the minimum pressure of the storm, while the simulations with the larger water depths show a much more suppressed increase. Regardless of depth, however, the presence of surface water is found to make landfall decay slower than a dry or moist land surface (Shen et al. 2002).

A TC's potential for maintaining or increasing its intensity over land is also a function of the underlying surface characteristics. For example, hot sandy soils may store enough heat to allow for the diffusion of heat upward at a rate fast enough to sustain warm-core storms of lower hurricane intensity (i.e., category 1 and 2 storms), succeeding the rain from an incoming cyclone (Emanuel et al. 2008). But, to support more intense storms, these same soils must not only be very warm, but also be able to keep a higher heat conductivity in the presence of increased moisture (Emanuel et al. 2008). However, soil moisture contributions from preceding months at the location(s) of interest may be more impactful to TC intensity than the moisture during the event (Evans et al. 2011). Specifically, the maintenance of boundary layer moisture over the preexisting soil moisture content is more connected to the final intensity of the simulated (and likely observed) vortices than an along-track TC rainfall mechanism like the one proposed by Emanuel et al. (2008), where they found the intensity of tropical systems decreases rapidly in the

presence of lower thermal diffusivity of the soil, as a result of lower rainfall rates (Evans et al. 2011).

While the ability to understand the characteristics that could lead to maintenance or intensification of overland TCs has improved, predicting the increases in/maintenance of TC intensity continues to be a challenge within the meteorological community. It has been documented that certain aspects of TC predictability, such as the storm track, have seen tremendous improvement, especially with the technological advances that we have witnessed since the turn of the century (Zhang and Tao 2013). However, while the ability to predict a TC's path has gotten better, intensity predictability has seen little to no improvement in skill for the last few decades (Zhang et al. 2014). The lack of improvement has been attributed to variety of factors, such as inadequate observations of the lower atmosphere and ocean (in both quantity and quality) and insufficiently robust algorithms to assimilate those observations (Emanuel and Zhang 2017). These issues ultimately lead to the practical predictability limit of TC intensity being only about three days (whereas the intrinsic predictability is approximately four to five days) and is highly variable between cases (Kieu and Moon 2016).

TC intensity itself is an important predictor in future intensity change (Fig. 2; Zhang et al. 2014). Errors resulting from misgauging of initial TC intensity are the dominant cause of errors for the first few days (Emanuel and Zhang 2017), especially when storms are of a lower intensity (Zhang and Emanuel 2016). The high sensitivity to initial intensity error (when it is small) could be due to the striking sensitivity of RI of a weak TC to shear (Zhang and Tao 2013; Tao and Zhang 2015; Emanuel and Zhang 2016). In other words, as initially stronger TCs tend to weaken in the forecasts, the associated intensity forecast errors generally decrease over time, whereas initially weaker TCs often have increasing intensities, leading to greater amounts of error at later lead times (Zhang et al. 2014). The presence of RI in the evolution of a TC in and of

itself is also important, as the largest errors in TC intensity forecasts are typically found during this period (Fig. 3; Judt et al. 2016). After the completion of RI, the spread becomes similar (and smaller) among all groups of ensembles, (Fig. 4; Zhang and Tao 2013).

Vertical wind shear (VWS) has also been shown to have dramatic influences on TC intensity predictability, particularly during the TC's formation and RI stages (Zhang and Tao 2013). Greater VWS magnitudes typically correspond to larger uncertainties in the intensity forecasts, in part due to differences in RI timing. For example, larger VWS – even when remaining small in magnitude – leads to greater ensemble spread during RI, and thus greater levels of uncertainty in forecast intensity (Zhang and Tao 2013). Also, VWS is initially uncorrelated and becomes strongly anticorrelated with TC intensity over time in initially weaker TCs, suggesting that the effects of VWS likely depend significantly on the TC's intensity (Sippel and Zhang 2008).

The chaotic nature of moist convection is also important to TC intensity predictability, as the evolution of forecast intensity is sensitive to both initial inner-core tropospheric moisture and wind fields. This implies that for reasonable estimates of magnitude, the initial inner-core moisture uncertainty could be a dominant source of forecast intensity error out to a few days lead time (Zhang and Tao 2013), after which free-tropospheric moisture outside the inner core would begin to play a role, if it can be ventilated into the inner core (by large VWS; Emanuel and Zhang 2017). In other words, while the final intensity of a TC is more weakly correlated with the initial water-vapor mixing ratio (through nearly the entire troposphere), a TC's initial intensity (and thus also its intensity in the first few days following TC genesis) is more strongly correlated to the water-vapor mixing ratio (hence the greater intensity error; Sippel and Zhang 2008). However, when there is little to no forecast spread among the available model guidance, especially in the TC's track, intensity forecasts are predominantly governed by both the initial inner-core dynamic and thermodynamic conditions. This is because while the initial inner-core

vortex intensity perturbations are extremely influential, there are still a number of uncertainties in the TC intensity forecasts using only the inner-core moisture perturbations. Furthermore, just retaining the inner-core moisture perturbations above the boundary layer and outside the eye will lead to considerable spread in the intensities (Emanuel and Zhang 2017).

It was also found that the divergence in intensity across members can be associated with differences in the timing and strength of each ensemble member's respective eyewall replacement cycles (ERCs). The secondary eyewall formation leads to the weakening of the radial inflow into the primary eyewall, subsequently weakening its convection and therefore the TC intensity (Judt et al. 2016).

Based on the knowledge (or lack thereof) that meteorologists have regarding overland TC maintenance and/or intensification, a hypothesis is formed to test our understanding. It is believed that because of the large sensitivity of TC forecasts to initial small-scale, finite amplitude perturbations in both atmospheric and thermodynamic fields, overland TC intensity change is as sensitive to initial atmospheric variability on the order of observation uncertainty as it is to disabling the leading physical processes governing surface energy exchange(s) in these TCs. A detailed description of the methodology is presented in section 2, followed by a short synopsis of the TC of interest (North Atlantic TC Erin of 2007) in section 3. Results are presented in section 4. Finally, a subsequent analysis, summary and conclusions are provided in section 5.

2. Methodology

a. Cycled Analysis

The setup largely follows that of Grunzke and Evans (2017), but for the location of interest (Oklahoma). DART (Manhattan Release), coupled with WRF-ARW version 4.4.1 (Skamarock et al. 2019), is employed to assimilate observations and create ensemble initial conditions (ICs) using an Ensemble Kalman Filter (EnKF). Cycled data assimilation starts at 0000 UTC 13 August 2007, advancing forward in 6 h increments until 0000 UTC 18 August 2007, when 50-member ensemble forecasts are then generated and deployed. The assimilation takes place on a domain centered over the contiguous United States, and includes parts of Canada, Mexico, the Atlantic and Pacific oceans, and the Gulf of Mexico (Fig. 9). There is 15-km horizontal grid spacing and 400 x 300 horizontal grid points, along with 50 vertical levels. The parameterizations used generally follow those of Davis et al. (2008) and are displayed in table 1.

To generate ensemble initial conditions for the first assimilation cycle, the 0000 UTC 13 August 2007 GFS analysis is perturbed using 50 random samples from the National Center for Environmental Prediction's (NCEP) background error covariance matrix (Torn et al. 2006, Barker et al. 2012). This is necessary to account for the uncertainty in the observations and the model itself. The lateral boundary conditions (LBCs) for the first and all subsequent data assimilation cycles are given by 0-h GFS analyses and 6-h GFS forecasts and are perturbed following a similar perturbation technique to that of Torn et al. (2006). Additionally, adaptive Gaspari-Cohn localization (Gaspari and Cohn 1999; Anderson 2012), and time- and space-varying adaptive prior inflation techniques (Anderson 2009) are applied to help with spurious correlation as a result of sampling errors and keep the ensemble spread (e.g., Torn 2010; Romine et al. 2013; Schwartz et al. 2014).

There are a number of assimilated observation types for a representative assimilation cycle (Fig. 10; Grunzke and Evans 2017). These observations include standard aviation routine weather reports [also known as METARs – which include measurements of horizontal (u) and vertical (v) velocity, temperature (T), altimeter (alt) and specific humidity (q)], marine stations (u, v, T, Alt, q) and profilers [u, v, Pressure (p)] (a more detailed list of observation types, assumed errors, and observation windows, is provided in table 2; Grunzke and Evans 2017). The model variables that are ultimately updated throughout the cycled analysis include U, V, W, T, T2, QVAPOR, Q2, QCLOUD, QRAIN, QNRAIN, QSNOW, QICE, QNICE, QGRAUP, H_DIATBATIC, REFL_10CM, PH, MU, U10, V10, and PSFC. The soil state (moisture, temperature, etc.) is replaced using soil data from the corresponding 0-h GFS analysis, in between the data assimilation cycle and the transition to the next model advance.

b. Free forecasts

Using the ICs given by the final cycled analysis from 0000 UTC 18 August 2007, a 50-member ensemble forecast is performed. These ensemble forecasts are run using a two-way nested domain with higher spatial resolution on the interior domain, which is important for capturing features such as rotating thunderstorms within the TC. The outer domain is set up as in the previous section, while the inner domain has 1101 x 1001 horizontal grid points, 3-km grid spacing, and 50 vertical levels. It is centered over the south-central US, extending from the Ohio River Valley westward, and from Montana southward, encompassing parts of Mexico, the Gulf of Mexico, and the eastern Pacific (Fig. 9). The LBCs are updated every 6-h using the data from the 0000 UTC 18 August 2007 forecast cycle of the NCEP GFS model that are perturbed with the previously mentioned fixed covariance perturbation technique of Torn et al. (2006). Outputs from the model(s) are generated hourly. The physical parameterizations used by the ensemble forecasts are almost identical to those of the cycled analysis system, but for the treatment of

convection, which is done explicitly on the forecast domain (similar to Romine et al. 2013, 2014, and Torn and Romine 2015, among others). This configuration is similar to past studies using DART (coupled with WRF-ARW) to create WRF-ARW ensemble of skillful, convection-allowing forecasts (e.g., Romine et al. 2013, 2014; Schwartz et al. 2014, 2015b,c; Torn and Romine 2015).

3. Erin Synopsis

Erin was initially classified as Tropical Depression Five (2007), which organized in the south-central Gulf of Mexico around 0000 UTC on 13 August 2007 (Arndt et al. 2009). By 15 August, the National Hurricane Center (NHC) upgraded the depression to Tropical Storm Erin as it moved northward. However, because of the short time that Erin spent over the Gulf of Mexico, combined with marginally favorable atmospheric conditions for TC intensification, Erin's 1-minute sustained 10-m winds over water were never greater than 18 m s^{-1} with a minimum sea level pressure no lower than 1003 hPa (Arndt et al. 2009). Erin eventually made landfall as a tropical depression at San Jose Island, Texas on the morning of 16 August.

Around the time that Erin made landfall and the subsequent days that followed, the synoptic environment across the U.S. Southern Great Plains was dominated by a strong midtropospheric sub-tropical ridge (Arndt et al. 2009). This subtropical ridge was the primary steering mechanism for Erin and its associated tropospheric moisture as the storm moved westward and eventually north through central and north-central Texas (Arndt et al. 2009).

As Erin moved through Texas on 17-18 August 2007, a gradual decay in the tropical characteristics begin to occur in the TC, culminating in the transition from a closed low (which is one of the most important defining characteristics of a TC; National Hurricane Center) to an open wave with a pronounced trough across the southern plains (Arndt et al. 2009). However, by the local evening of 18 August and into the early morning hours of 19 August, TC Erin began to

dramatically intensify over Oklahoma, despite being almost 500 mi (in linear distance) from landfall, and traveling almost 700 miles on a curved, overland path (Monteverdi and Edwards 2010). Associated with the increase in intensity was a reduction in minimum sea-level pressure from 1007 to 995 hPa and an increase in 1-min maximum sustained 10-m wind speed from 20 kt to 50 kt (both of which are more intense than any observed while Erin still retained its tropical status; Brennan et al. 2009; Evans et al. 2011). Additionally, the reintensification of the remnants of Erin produced an almost eye-like feature over Oklahoma, which was captured using the Weather Surveillance Radar – 1988 Doppler (WSR-88; Evans et al. 2011).

While most agree that TC Erin strengthened while over land, the reasons behind this intensification differ slightly between studies. For instance, there is some belief that Erin's reintensification was strongly influenced by the interaction of the remnants of Erin and the associated warm, moist air mass with both the ambient environmental conditions and ascent from a midlevel shortwave trough, coupled with a release of latent heat (Arndt et al. 2009, Monteverdi and Edwards 2010). Another common theme across many studies (Arndt et al. 2009, Monteverdi and Edwards 2010, Evans et al. 2011, Kellner et al. 2012) is that the underlying surface conditions were an important feature of TC Erin's intensification. More specifically, TC development seems more likely over land when the underlying surface is both moist and has a high heat conductivity (Evans et al. 2011, Kellner et al. 2012). But, while there are different explanations for why this event occurred, the general consensus is that an anomalously wet land surface (along with an anomalously warm air mass), as seen in Oklahoma during TC Erin, is vital for maintaining or intensifying future overland TCs or their remnants (Emanuel et al. 2008, Arndt et al. 2009, Monteverdi and Edwards 2010, Evans et al. 2011, and Kellner et al. 2012). This work aims to build upon these ideas.

4. Results

a. Data Assimilation Performance

Here, different surface and vertical level observation types are plotted for both the prior and posterior analyses to compare the observation diagnostics at each analysis time. Optimal performance is achieved when the RMSE and spread are close in magnitude to each other, which could be indicative of well-tuned observation error statistics (Romine et al. 2013). Additionally, the assimilation quality is 'better' when the observation RMSE and total spread minimally vary with time.

For many surface-level observation platforms, the root-mean-square-error (RMSE), total spread, and bias are reduced for the posterior compared to the prior at each analysis time (Fig. 11). In the observation types of 10-m wind and temperature, there is a small, but nonetheless noticeable difference between the posterior and prior biases, where the prior has a generally larger (absolute) bias compared to the posterior. The discrepancy is larger when considering prior and posterior biases of the altimeter observation type. Here, the prior bias clearly has a larger absolute value when compared to the posterior and reaches a magnitude of nearly 8 meters by the end of the observation period. Additionally, while the value of RMSE and total spread are similar across observation types and times, most notably near the final cycled analysis time, the magnitudes of those observation types seem to change with time. This is most notable when considering the altimeter observation type, which has magnitudes as high as 6 meters early on in the cycled analysis and reaches as high as 8 meters by the end of the cycled analysis period (0000 UTC on 18 August 2007). These discrepancies are also more pronounced in the prior compared to the posterior values. Beyond that, a cool and (slight) moist bias is also evident but seem to be out of phase temporally with each other. Therefore, it is hard to determine whether these biases may be reflective of the well-documented cool/moist bias in pre convective

boundary layers of the MYJ (e.g., Coniglio et al. 2013). Lastly, there is a slight easterly bias present in both the 10-m horizontal and meridional wind components.

The vertical profile observation platforms also show a similar depiction and performance to the surface-level platforms (Fig. 12). There is generally a good agreement between the RMSE and spread, which could also be indicative of well-tuned observation error statistics (Romine et al. 2013). Additionally, the posterior analysis reduces the magnitude of the RMSE and total spread, respectively. However, there are some observation diagnostics, such as the U- and V-Wind components of the Radiosonde, Satellite, and ACARS observation types, respectively, where the total spread is larger relative to RMSE, a situation that corresponds to ensemble analyses being overdispersive relative to the observations. This suggests that reducing the assumed observation errors or decreasing the initial ensemble spread could lead to better assimilation-system performance for these variables. There are also some instances where the posterior values are generally larger than those of the prior, especially when considering the biases of the different observation types, and this is evident in many of the wind components of the respective platforms.

b. Ensemble Performance and Composites

Along with the evaluation of different observation diagnostics, a comprehensive analysis of ensemble outputs is conducted (Figs. 13, 14). Members are categorized into GOOD and BAD members, to help delineate which members best represent Erin’s intensity late on 18 August and the early hours of 19 August 2007 (Figs. 15, 16). To further rationalize the selection of "GOOD" and "BAD" ensemble members to assess Erin's intensification and predictability, it is important to understand the ensemble's fundamental characteristics. To that point, a comprehensive analysis of ensemble outputs is conducted (Figs. 13,14) to provide a nuanced understanding of Erin's representation in the ensemble forecast. Two 25-panel plots are introduced, illustrating the

variations across the 50-member ensemble and serve as a visual aid in comprehending the ensemble's collective portrayal of Erin's characteristics. There is not a stringent threshold for defining "GOOD" members based solely on simulated Erin's reintensification, due to the ensemble's demonstrated challenges, uncertainties, and variabilities of each member, which impact its ability to reliably capture Erin's intensification dynamics. These complexities should be acknowledged to contextualize the subsequent analysis of "GOOD" and "BAD" members' performance and their implications of characteristics associated with Erin's forecast.

Firstly, the GOOD and BAD members are determined with the help of MSLP, where the good members display at least one closed isobar for an extended period of time in the simulation, and bad members experience near-immediate dissipation. Once these members are determined, a number of model variables are selected at different pressure levels and evaluated for their accuracy based on observed atmospheric phenomena at different observation times. The differences between these members are then plotted and compared, where red shading indicates a stronger magnitude of the GOOD members and blue represents a stronger magnitude of the BAD members. In this case, 20 ensemble members are selected for this analysis, dividing them into 10 "GOOD" and 10 "BAD" members. Anomalies described in the subsequent paragraphs are defined as the difference between GOOD and BAD composite means.

The indicated forecast from the 10-m wind speeds suggests that the GOOD members display a more organized and stronger storm as compared to the BAD members. This is evidenced by stronger wind speeds, and those winds being concentrated in the right quadrants of the storm, which are typically the location of the strongest winds in a TC and will be discussed further.

In the early stages of the simulation, the BAD ensemble members appear to outperform the GOOD ensemble members, particularly around hours 9-15 (Fig. 17a,b,c,d) and across various pressure levels, such as 850 and 700 hPa, as evidenced by the presence of negative differences or

contrasts (Fig. 17e,f). However, as the simulation progresses, distinctions in wind speeds between the datasets start to reveal the basic shape of the TC, with wind barbs displaying a counterclockwise direction, indicating of cyclonic rotation. Additionally, as the simulation advances, the wind speeds of the GOOD members consistently surpass those of the BAD, suggesting they may forecast of a more robust system. Towards the end of the simulation period, a discernible pattern emerges, with positive wind differences associated with the GOOD members being greatest on the right side(s) of the TC, while the largest BAD member differences are mostly on the left side(s). As this is in line with the typical distribution of strongest winds in a TC, these results suggest the idea that the GOOD members may provide a more accurate representation of the TC (NOAA 2023). An exception occurs at 500mb, where the pattern is somewhat reversed towards the end of the simulation period, indicating that the simulation may perform better at forecasting winds at lower levels.

Sea level pressure (SLP) is another critical element to analyze. Initially, SLP is higher in the GOOD members (Fig. 18), but by the end of the simulation, the BAD members exhibit large magnitudes in and around the expected location of Erin, potentially indicating a forecast of a stronger storm by the GOOD members, as lower SLP values are typically associated with stronger cyclones (Atkinson and Holliday 1977).

At 500 hPa geopotential heights (which are typically the best heights to help understand the links between large-scale weather patterns, like tornadoes, or in this case, a cyclone; Moore and Dixon 2014), the GOOD members show a slightly amplified trough around Erin as it progresses inland compared to the BAD members, as indicated by negative geopotential heights throughout much of the simulation (Fig. 19). As the trough is tied to Erin rather than the surrounding environment, this reflects a stronger, more vertically coherent circulation of Erin.

Furthermore, the mixing ratio values of the GOOD members indicate a more robust system in comparison to the BAD members, as illustrated in Figures 20 and 21. The collective trend reveals a positive anomaly, indicative of GOOD members, moving in tandem with the storm as it progresses inland. While the temporal alignment of these patterns varies at different altitudes, an overall northwesterly flow of positive anomalies is evident across the observation heights. This observation aligns with the expectation that a stronger system is associated with increased moisture. Notably, differences in mixing ratio magnitudes are more pronounced at lower levels, signifying a heightened presence of moisture at those altitudes. It is important to note that moisture levels in the mid and upper troposphere are generally higher in the GOOD members compared to the BAD members, a condition conducive to tropical cyclone development and maintenance (NOAA 2023). However, it is crucial to interpret these differences comprehensively, as larger mixing ratios alone do not necessarily indicate a stronger cyclone from a physical standpoint. While larger mixing ratios are likely associated with greater available latent heating, it is essential to consider that the realization of latent heating, achieved by lifting parcels to saturation, is a prerequisite for impacting the cyclone's intensity.

5. Discussion and Conclusion

This research examined the predictability and dynamics of tropical cyclones that reintensify or maintain their intensity over land in weakly or non-baroclinic environments, using TC Erin (2007) as a proxy. For all the surface level observations considered, the root-mean-square-error (RMSE), total spread, and bias are reduced for the posterior compared to the prior at each analysis time (Grunzke and Evans 2017). The vertical profile observations generally exhibit similar characteristics and have good agreement between bias and total spread, which can be

indicative of well-tuned observation error statistics, with a near zero bias (Romine et. al 2013, Grunzke and Evans 2017).

The wind speed anomalies also suggest that the GOOD members perform better compared to the BAD, as their differences are more concentrated in the right quadrants of the storm, where stronger winds would typically be expected to be in a TC (NOAA 2023). Additionally, the upper-level trough present in the 500 hPa geopotential height plots reflects a stronger, more vertically coherent Erin circulation.

Overland TC model performance has been the subject of numerous past studies (e.g., Shen et al. 2002, Emanuel et al. 2008, Evans et al. 2011, Chen and Chavas 2020, and Hlywiak and Nolan 2021) as meteorologists continue to try and understand the conditions that cause the storms to behave in a certain way (in this case, dealing with maintenance). While this study contributes to the ongoing efforts to enhance practical predictability by reducing error magnitudes, it is important to acknowledge existing limitations. The methodology used in this study relies on a relatively 'weak' threshold for defining good members, where good members are identified based on the presence of at least one closed isobar, and bad members correspond to near-immediate dissipation. A deeper understanding of the ensemble forecast characteristics is crucial for contextualizing the chosen threshold. The ensemble used in this study also has inherent issues that limit its utility in studying Erin's intensification and predictability. For example, past studies indicate there may be a bifurcation point that is reached with some of these atmospheric observations, meaning that any further analysis error reduction would not lead to any improvements in predictability (Melhauser and Zhang 2012, Grunzke and Evans 2017). So, while reducing the large scale error could have the potential to improve the forecast of the overland TC, the extent reducing large-scale or small-scale errors to improve overland TC forecasts is unknown for different observation types (Grunzke and Evans 2017). More

information is needed to understand whether there truly is a bifurcation point with these ensemble member forecasts and observation types, and if there is, how it can be determined when it is reached. Addressing these limitations and improving ensemble performance are ongoing efforts.

References

Ancell, B. C., 2013: Nonlinear characteristics of ensemble perturbation evolution and their application to forecasting high-impact events. *Wea. Forecasting*, **28**, 1353–1365, https://doi.org/10.1175/WAF-D-12-00090.1.

Ancell, B. C., and A. A. Coleman, 2022: New perspectives on ensemble sensitivity analysis with applications to a climatology of severe convection. *Bull. Amer. Meteor. Soc.*, **104**, 511–530, https://doi.org/10.1175/BAMS-D-20-0321.1.

Ancell, B. C., and C. F. Mass , 2006: Structure, growth rates, and tangent linear accuracy of adjoint sensitivities with respect to horizontal and vertical resolution. *Mon. Wea. Rev.*, **134**, 2971– 2988, https://doi.org/10.1175/MWR3227.1.

Arndt, D. S., J. B. Basara, R. A. McPherson, B. G. Illston, G. D. McManus, and D. B. Demko, 2009: Observations of the overland reintensification of Tropical Storm Erin (2007). *Bull. Amer. Meteor. Soc.*, **90**, 1079–1093, https://doi.org/10.1175/2009BAMS2644.1.

Atkinson, G. D., and C. R. Holliday, 1977: Tropical cyclone minimum sea level pressure/maximum sustained wind relationship for the western North Pacific. *Mon. Wea. Rev.*, **105**, 421–427, https://doi.org/10.1175/1520-0493(1977)105<0421:TCMSLP>2.0.CO;2.

Barker, D. M., and Coauthors, 2012: The Weather Research and Forecasting Model's Community Variational/Ensemble Data Assimilation System: WRFDA. *Bull. Amer. Meteor. Soc.*, **93**, 831–843, https://doi.org/10.1175/BAMS-D-11-00167.1.

Chang, E. K. M., M. Zhang , and K. Raeder , 2013: Medium-range ensemble sensitivity analysis of two extreme Pacific extratropical cyclones. *Mon. Wea. Rev.*, 141, 211– 231, https://doi.org/10.1175/MWR-D-11-00304.1.

Chen, J., and D. R. Chavas, 2020: The transient responses of an axisymmetric tropical cyclone to instantaneous surface roughening and drying. *J. Atmos. Sci.*, ***77***, 2807–2834, https://doi.org/10.1175/JAS-D-19-0320.1.

Chih, C. H., K. H. Chou, and C. C. Wu, 2022: Idealized simulations of tropical cyclones with thermodynamic conditions under reanalysis and CMIP5 scenarios. *Geo. Sci. Letters*, **9**, 1–20, https://doi.org/10.1186/s40562-022-00239-6.

Coleman, A. A., and B. C. Ancell, 2020: Toward the improvement of high-impact probabilistic forecasts with a sensitivity-based convective-scale ensemble subsetting technique. *Mon. Wea. Rev.*, 148, 4995– 5014, https://doi.org/10.1175/MWR-D-20-0043.1.

Coniglio, M. C., J. Correia Jr., P. T. Marsh, and F. Kong, 2013: Verification of convection-allowing WRF Model forecasts of the planetary boundary layer using sounding observations. *Wea. Forecasting*, **28**, 842–862, doi:10.1175/WAF-D-12-00103.1.

Davis, C., and Coauthors, 2008: Prediction of landfalling hurricanes with the advanced hurricane WRF model. *Mon. Wea. Rev.*, **136**, 1990–2005, https://doi.org/10.1175/2007MWR2085.1.

Emanuel, K., and F. Zhang, 2016: On the predictability and error sources of tropical cyclone intensity forecasts. *J. Atmos. Sci.*, **73**, 3739–3747, https://doi.org/10.1175/JAS-D-16-0100.1.

Emanuel, K., and F. Zhang, 2017: The role of inner-core moisture in tropical cyclone predictability and practical forecast skill. *J. Atmos. Sci.*, **74**, 2315–2324, https://doi.org/10.1175/JAS-D-17-0008.1.

Emanuel, K., J. Callaghan, and P. Otto, 2008 A hypothesis for the redevelopment of warm-core cyclones over Northern Australia. *Mon. Wea. Rev.*, **136**, 3863–3872, https://doi.org/10.1175/2008MWR2409.1.

Evans, C., R. S. Schumacher, and T. J. Galarneau, 2011: Sensitivity in the overland reintensification of tropical cyclone Erin (2007) to near-surface soil moisture characteristics. *Mon. Wea. Rev.*, **139**, 3848–3870, https://doi.org/10.1175/2011MWR3593.1.

Grunzke, C. T., and C. Evans, 2017: Predictability and dynamics of warm-core mesoscale vortex formation with the 8 May 2009 “Super Derecho” event. *Mon. Wea. Rev.*, **145**, 811–832, https://doi.org/10.1175/MWR-D-16-0217.1.

Ha, S.-Y., and C. Snyder, 2014: Influence of surface observations in mesoscale data assimilation using an ensemble Kalman filter. *Mon. Wea. Rev.*, **142**, 1489–1508, doi:10.1175/MWR-D-13-00108.1.

Hawblitzel, D. P., F. Zhang, Z. Meng, and C. A. Davis, 2007: Probabilistic evaluation of the dynamics and predictability of the mesoscale convective vortex of 10–13 June 2003. *Mon. Wea. Rev.*, **135 ,** 1544–1563, https://doi.org/10.1175/MWR3346.1.

Hill, A. J., C. C. Weiss, and D. C. Dowell, 2021: Influence of a portable near-surface observing network on experimental ensemble forecasts of deep convection hazards during VORTEX-SE. *Wea. Forecasting*, **36**, 1141-1167, https://doi.org/10.1175/WAF-D-20-0237.1.

Hlywiak, J., and D. S. Nolan, 2021: The response of the near-surface tropical cyclone wind field to inland surface roughness length and soil moisture content during and after landfall. *J. Atmos. Sci.*, **78**, 983–1000, https://doi.org/10.1175/JAS-D-20-0211.1.

Hong, S. Y., and J. O. J. Lim, 2006: The WRF single–moment 6–class microphysics scheme (WSM6). *J. Korean Meteor. Soc.*, **42**, 129–151.

Hong, S. Y., Y. Noh, and J. Dudhia, 2006: A new vertical diffusion package with an explicit treatment of entrainment processes. *Mon. Wea. Rev.*, **134**, 2318–2341, https://doi.org/10.1175/MWR3199.1.

Iacono, M. J., J. S. Delamere, E. J. Mlawer, M. W. Shephard, S. A. Clough, and W. D. Collins, 2008: Radiative forcing by long–lived greenhouse gases: Calculations with the AER radiative transfer models. *J. Geophys. Res.*, **113**, D13103. https://doi.org/10.1029/2008JD009944.

Judt, F., S. S. Chen, and J. Berner, 2016: Predictability of tropical cyclone intensity: scale-dependent forecast error growth in high-resolution stochastic kinetic energy backscatter ensembles. *Quart. J. Roy. Meteor. Soc.,* **142**, 43–57, https://doi.org/10.1002/qj.2626.

Kellner, O., D. Niyogi, M. Lei, and A. Kumar, 2012: The role of anomalous soil moisture on the inland reintensification of Tropical Storm Erin (2007). *Nat. Hazards*, **63**, 1573–1600, https://doi.org/10.1007/s11069-011-9966-6.

Kieu, C., and Z. Moon, 2016: Hurricane intensity predictability. *Bull. Amer. Meteor. Soc.*, **97**, 1847–1857, https://doi.org/10.1175/BAMS-D-15-00168.1.

Kuo, Y.-H., T.-K. Wee, S. Sokolovskiy, C. Rocken, W. Schreiner, D. Hunt, and R. A. Anthes, 2004: Inversion and error estimation of GPS radio occultation data. *J. Meteor. Soc. Japan*, **82**, 507–531, doi:10.2151/jmsj.2004.507.

Landsea, C. W., 2000: Climate variability of tropical cyclones: Past, present and future. *Storms*, **1**, 220–241.

Monteverdi, J. P., and R. Edwards, 2010: The redevelopment of a warm-core structure in Erin: A case of inland tropical storm formation. *Electron. J. Severe Storms Meteor.*, **5** (6), 1–18.

Moore, T. W., and R.W. Dixon, 2014: Patterns in 500 hPa geopotential height associated with temporal clusters of tropical cyclone tornadoes. *Meteor. Appl. Roy. Meteor. Soc.*, **22**, 314-322, 10.1002/met.1456.

National Hurricane Center: Tropical cyclone climatology. Accessed 3 April 2023, https://www.nhc.noaa.gov/climo/.

Romine, G. S., C. S. Schwartz, C. Snyder, J. L. Anderson, and M. L. Weisman, 2013: Model bias in a continuously cycled assimilation system and its influence on convection-permitting forecasts. *Mon. Wea. Rev.*, **141**, 1263–1284, https://doi.org/10.1175/MWR-D-12-00112.1.

Romine, G. S., C. S. Schwartz, J. Berner, K. R. Fossell, C. Snyder, J. L. Anderson, and M. L. Weisman, 2014: Representing forecast error in a convection-permitting ensemble system. *Mon. Wea. Rev.*, **142**, 4519–454, https://doi.org/10.1175/MWR-D-14-00100.1.

Schwartz, C. S., G. S. Romine, R. A. Sobash, K. R. Fossell, and M. L. Weisman, 2015a: NCAR's experimental real-time convection-allowing ensemble prediction system. *Wea. Forecasting*, **30**, 1645–1654, doi:10.1175/WAF-D-15-0103.1.

Schwartz, C. S., G. S. Romine, M. L. Weisman, R. A. Sobash, K. R. Fossell, K. W. Manning, and S. B. Trier, 2015b: A real-time convection-allowing ensemble prediction system initialized by mesoscale ensemble Kalman filter analysis. *Wea. Forecasting*, **30**, 1158–1181, doi:10.1175/WAF-D-15-0013.1.

Shen, W., I. Ginis, and R. E. Tuleya, 2002: A numerical investigation of land surface water on landfalling hurricanes. *J. Atmos. Sci.*, **59**, 789–802, https://doi.org/10.1175/1520-0469(2002)059<0789:ANIOLS>2.0.CO;2.

Sippel, J. A., and F. Zhang, 2008: A probabilistic analysis of the dynamics and predictability of tropical cyclogenesis. *J. Atmos. Sci.*, **65**, 3440–3459. https://doi.org/10.1175/2008JAS2597.1.

Shamarock, W. C., and Coauthors, 2019: A description of the Advanced Research WRF version 4. *NCAR Tech. Note*, NCAR/TN-556+STR, 162 pp. doi:10.5065/1dfh-6p97.

Tewari, M., F. Chen, W. Wang, J. Dudhia, M. A. LeMone, K. Mitchell, M. Ek, G. Gayno, J. Wegiel, and R. H. Cuenca, 2004: Implementation and verification of the unified NOAH land surface model in the WRF model. *20th Conference on Weather Analysis and Forecasting/16th Conference on Numerical Weather Prediction*, pp. 11–15.

Thompson, G., P. R. Field, R. M. Rasmussen, and W. D. Hall, 2008: Explicit forecasts of winter precipitation using an improved bulk microphysics scheme. Part II: Implementation of a new snow parameterization. *Mon. Wea. Rev.*, **136**, 5095–5115. doi:10.1175/2008MWR2387.1.

Torn, R. D., G. J. Hakim, and C. Snyder, 2006: Boundary conditions for limited-area ensemble Kalman filters. *Mon. Wea. Rev.*, **134**, 2490–2502, https://doi.org/10.1175/MWR3187.1.

Torn, R. D., and G. S. Romine, 2015: Sensitivity of central Oklahoma convection forecasts to upstream potential vorticity anomalies during two strongly forced cases during MPEX. *Mon. Wea. Rev.*, **143**, 4064–4087, https://doi.org/10.1175/MWR-D-15-0085.1.

Tuleya, R. E., 1994: Tropical storm development and decay: sensitivity to surface boundary conditions. *Mon. Wea. Rev.*, **122**, 291–304, https://doi.org/10.1175/1520-0493(1994)122<0291:TSDADS>2.0.CO;2.

Wilcoxon, F., 1945: Individual comparisons by ranking methods. Biom. Bull., 1, 80–83.

Wilks, D. S., 2011: Statistical Methods in the Atmospheric Sciences (3rd Ed.). Academic Press, 704 pp.

Zhang, C., and Y. Wang, 2017: Projected Future Changes of Tropical Cyclone Activity over the Western North and South Pacific in a 20-km-Mesh Regional Climate Model. *J. Climate*, **30**, 5923–5941, https://doi.org/10.1175/JCLI-D-16-0597.1.

Zhang, F., and D. Tao, 2013: Effects of vertical wind shear on the predictability of tropical cyclones. *J. Atmos. Sci.*, **70**, 975–983, https://doi.org/10.1175/JAS-D-12-0133.1.

Zhang, Y., Z. Meng, F. Zhang, and Y. Weng, 2014: Predictability of tropical cyclone intensity evaluated through 5-yr forecasts with a convection-permitting regional-scale model in the Atlantic basin. *Wea. Forecasting*, **29**, 1003–1023, https://doi.org/10.1175/WAF-D-13-00085.1.

Appendix A: Figures

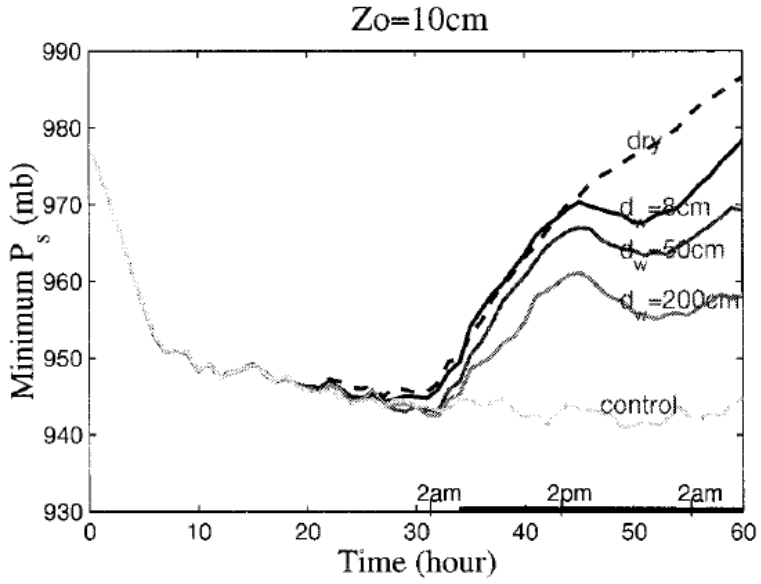

Figure 1: Hurricane intensity as a function of pressure over a 60-hour integration period for varying surface conditions. Here, d_w corresponds to water depth, and a constant surface roughening of Z_0 = 10 cm is used. The solid black line along the x-axis indicates the landfall, approximately 34 hours after the initialization of the various simulations. (Shen et. al 2002, Fig. 4)

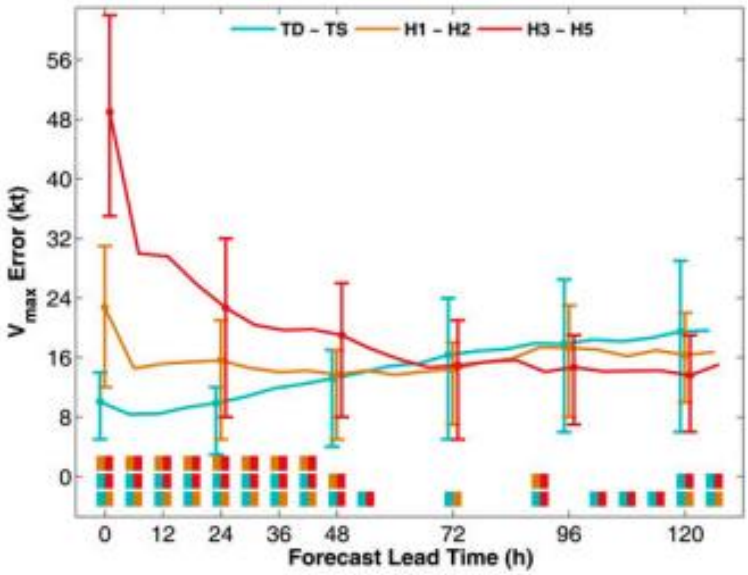

Figure 2: Mean absolute intensity forecast errors, based on the different best-track TC intensity categories. (Zhang et. al 2014, Fig. 4a)

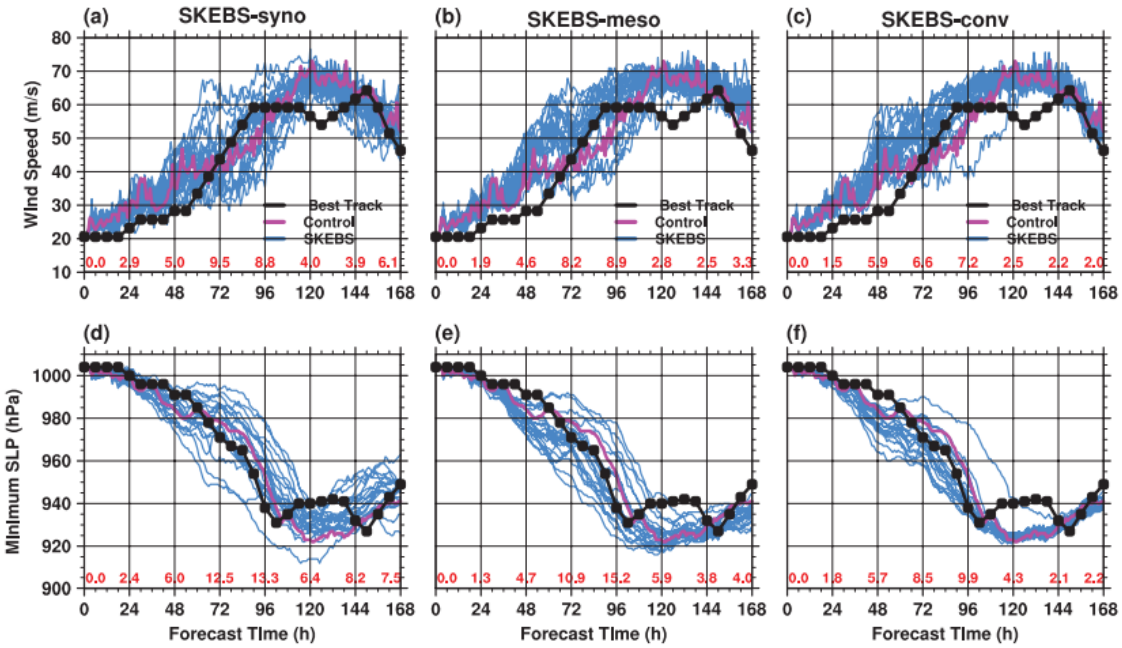

Figure 3: Best track position estimates (black contours) and 7-day forecasts of (a-c) maximum wind speed and (d-f) minimum sea level pressure. (Judt et al. 2016, Fig. 4)

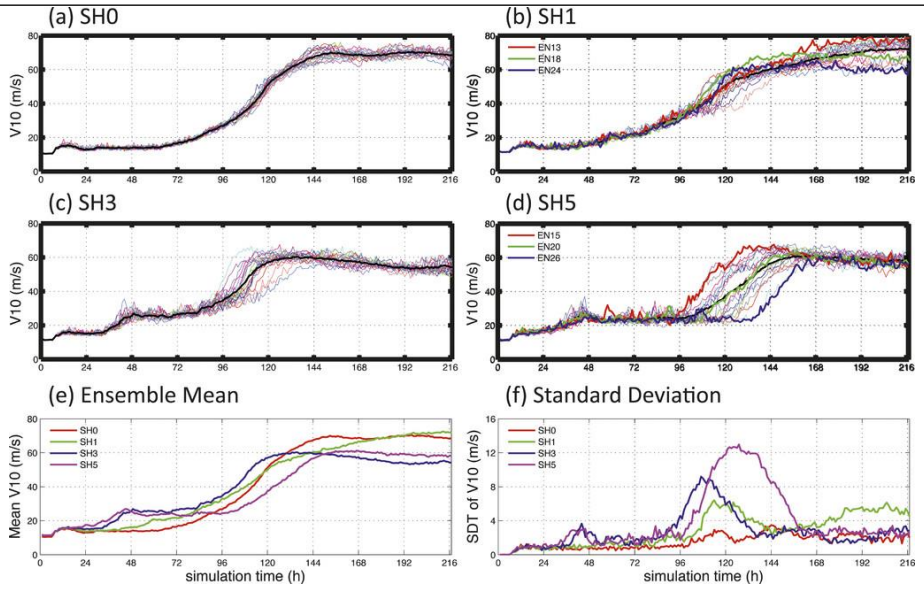

Figure 4: Time evolution of the TC intensity in terms of maximum 10-m wind speed for all ensemble members of SH0 (a), SH1 (b), SH3 (c), and SH5 (d), along with the ensemble mean (e) and the standard deviation (ensemble spread) from all ensemble experiments. (Zhang and Tao 2013, Fig. 2)

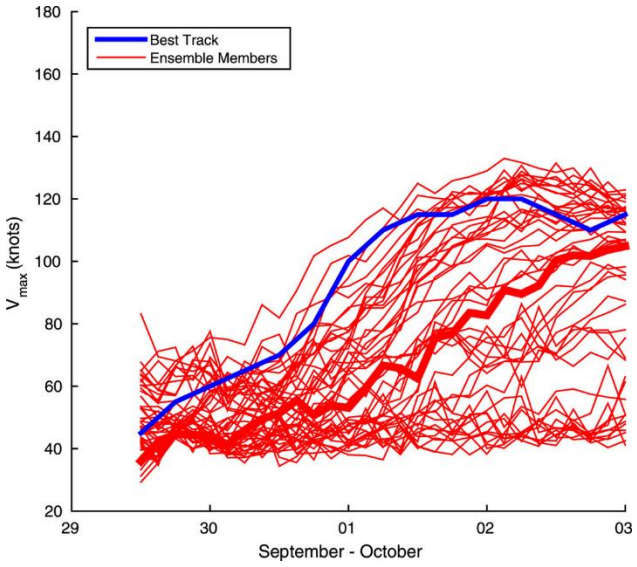

Figure 5: The intensity forecast of the WRF ensemble using only the PSU WRF-EnKF real-time ensemble analysis perturbations in the inner core region. (Emanuel and Zhang 2017, Fig. 3)

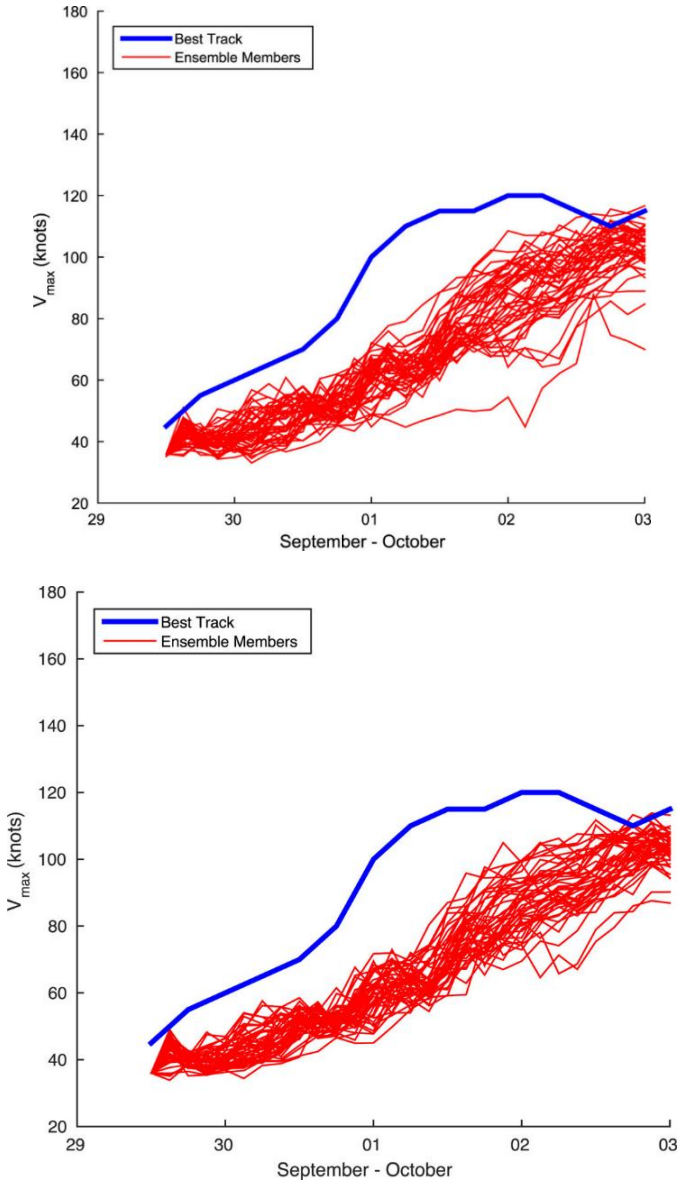

Figure 6: The intensity forecast of the WRF ensemble using only the PSU WRF-EnKF real-time ensemble analysis perturbations in the inner core region but retaining only the inner core moisture perturbations (a), or only using initial inner-core moisture perturbations above the boundary layer (b). (Emanuel and Zhang 2017, Figs. 4 and 5)

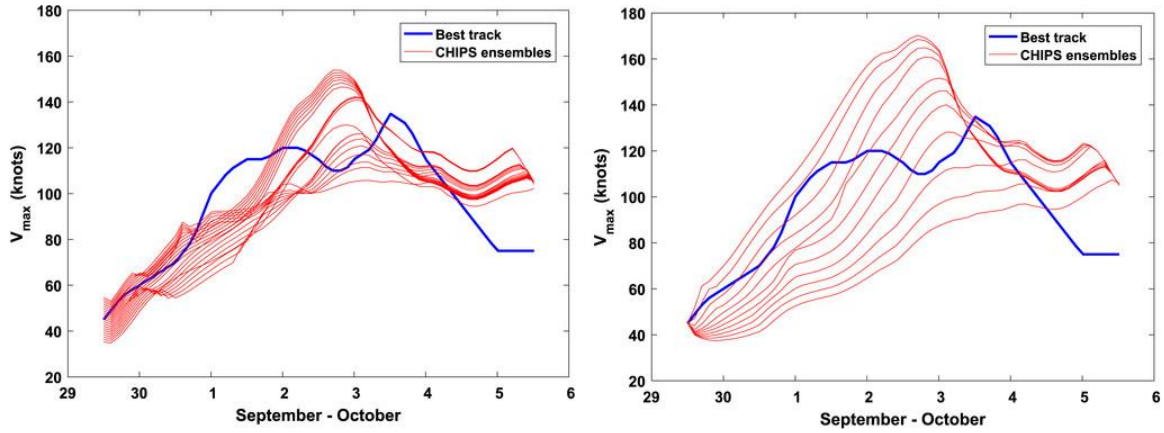

Figure 7: Evolution of CHIPS hindcasts of Joaquin (red), compared to the best track intensity (blue). Each hindcasts is initialized with (a) the initial wind speed varying by ± 5 m s^{-1} from the initial best track value, or (b) each hindcast in initialized with the observed wind speed. (Emanuel and Zhang 2017, Fig. 6)

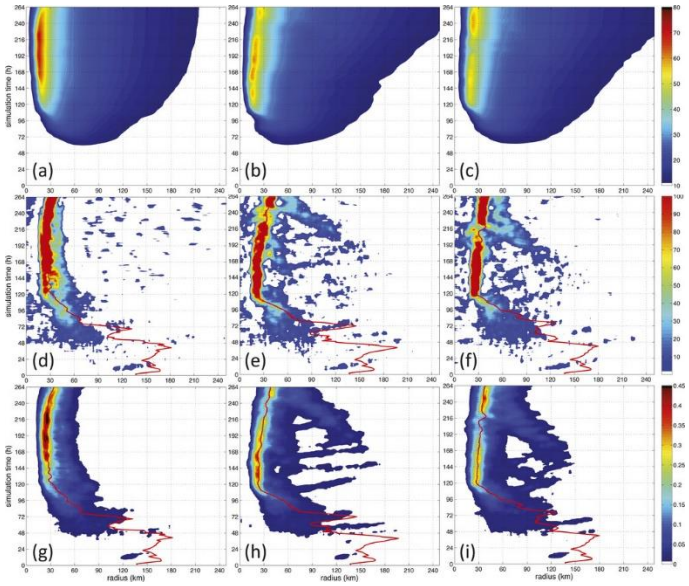

Figure 8: Time evolution of azimuthally averaged (a-c) tangential 10-m wind, (d-f) 500-hpa vertical wind, and (g-i) column-integrated positive-only diabatic heating rate for ensemble members EN13 (left), EN18 (middle), and EN24 (right). (Zhang and Tao, Fig. 7)

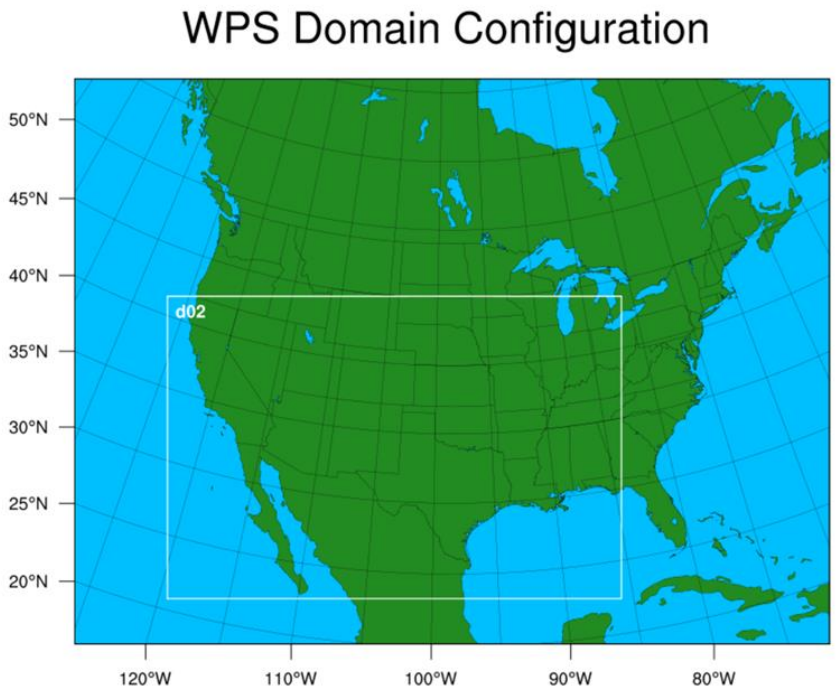

Figure 9: An example of the assimilation domain, where d02 represents the inner domain only used for free forecasts.

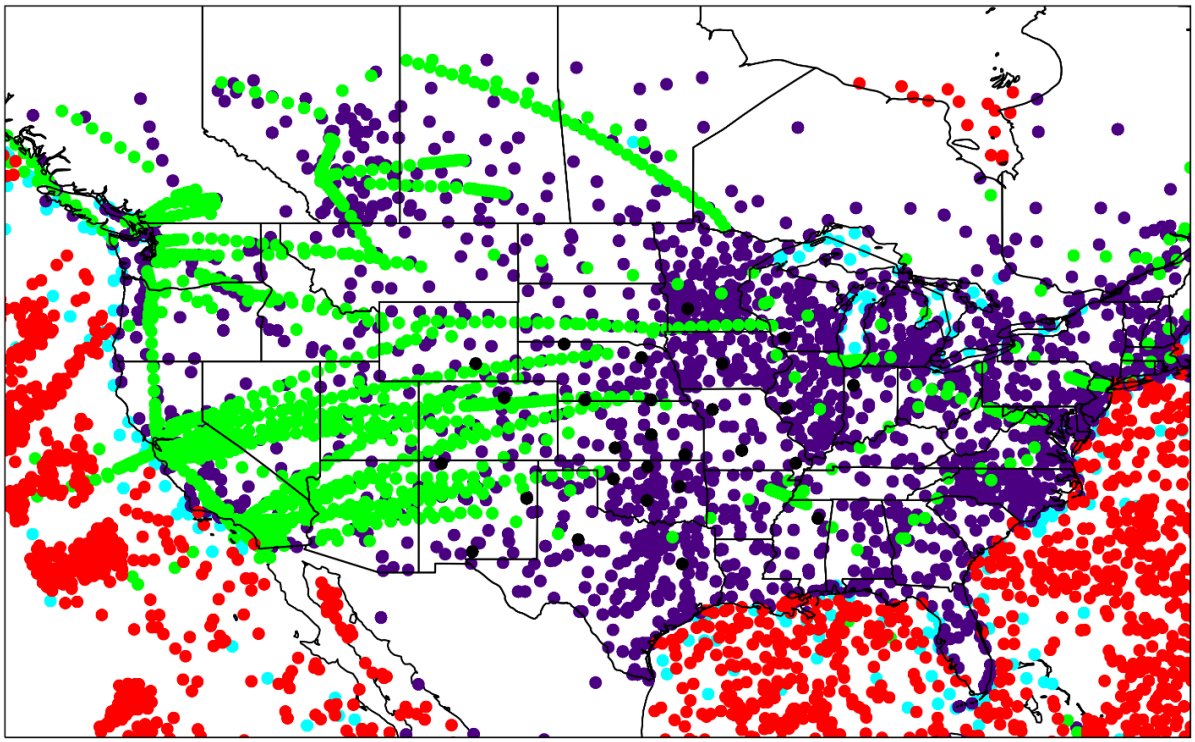

Figure 10: A distribution of the different assimilated observation platforms for a 0000 UTC 18 August 2007 analysis cycle, where the red dots represent satellite winds, the green dots represent the ACARs platform, the blue dots represent the marine platforms, the magenta dots represent the Radiosonde platform, purple dots represent the METAR platform, and the black dots represent the profiler platforms

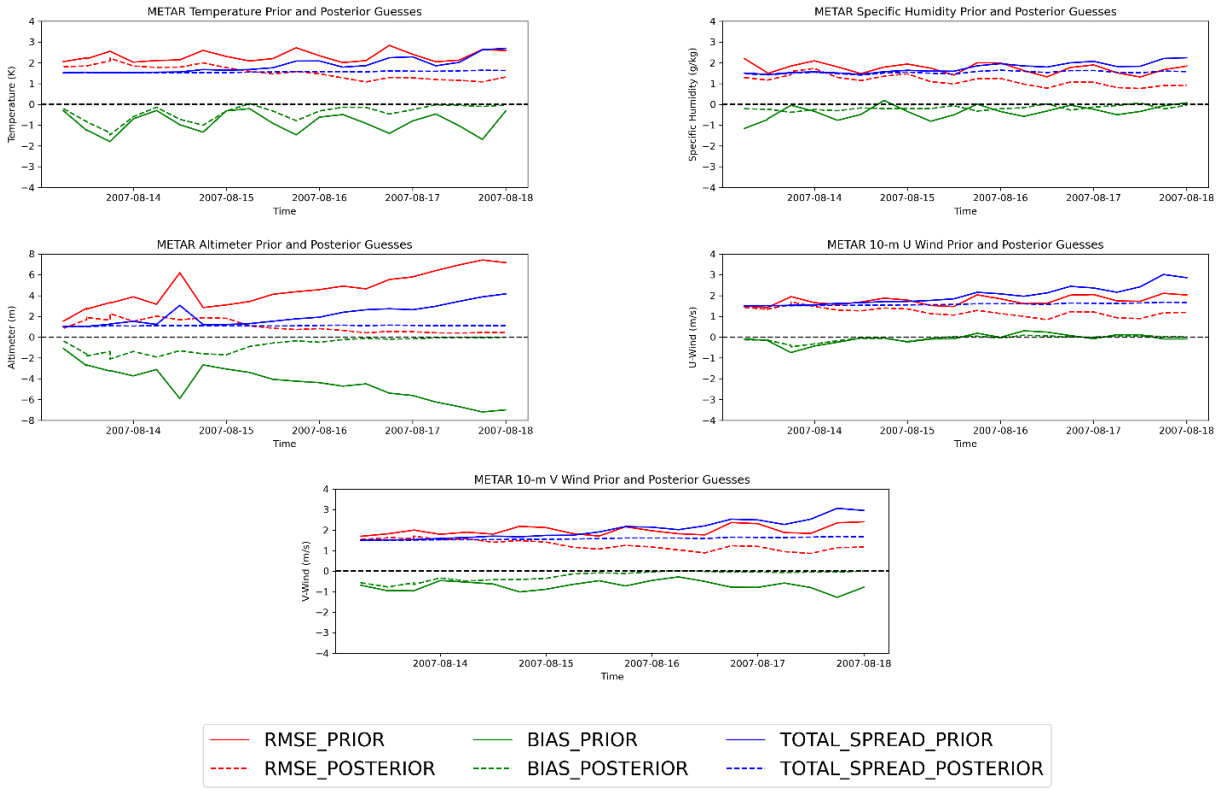

Fig 11: RMSE (red), total spread (blue), and bias (green) of the prior (dashed) and posterior (solid) ensemble estimates for METAR (a) temperature (K), (b) specific humidity (g kg^{-1}), (c) altimeter (hPa), (d) u (m s^{-1}), and (e) v (m s^{-1}) observations between 0000 UTC 13 August and 0000 UTC 18 August 2007.

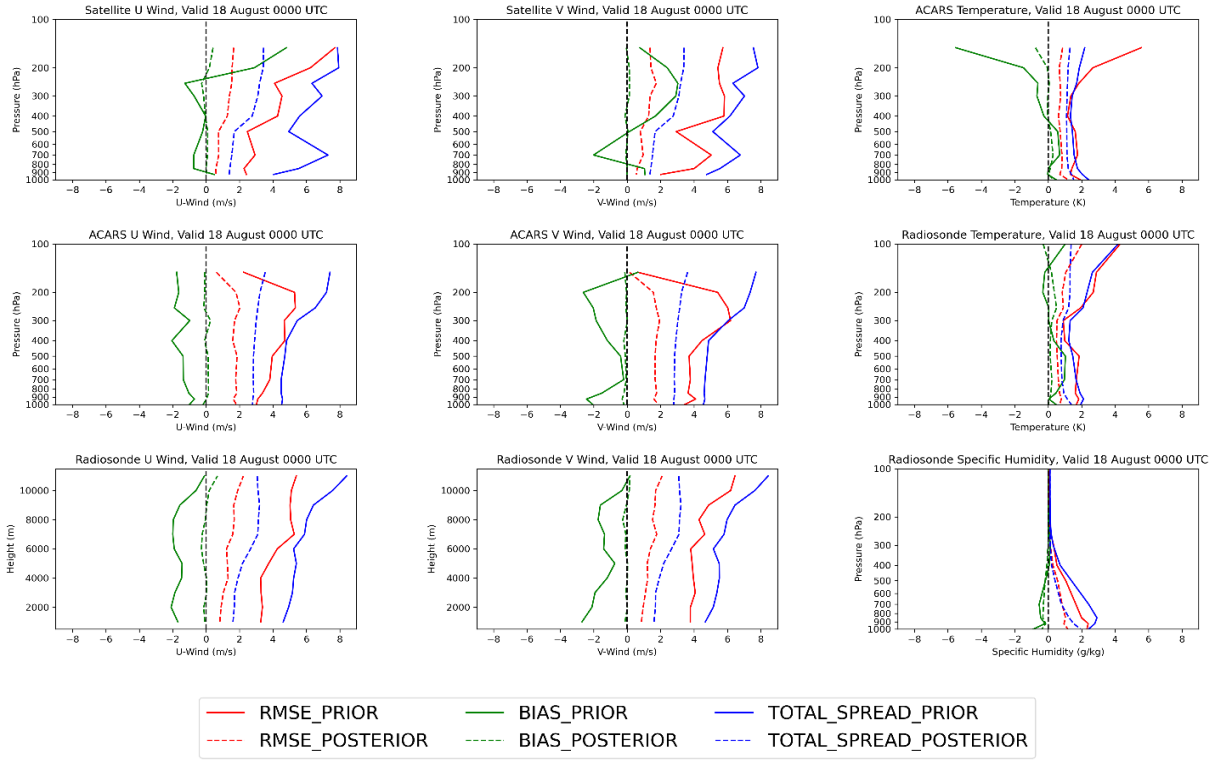

Fig. 12: RMSE (red), total spread (blue), and bias (green) of the posterior (dashed) and prior (solid) ensemble analysis at 0000 UTC 18 August 2007 for AMV (a) *u* wind (m s^{-1}), and (b) *v* wind (m s^{-1}) ; ACARS (c) temperature (K), (d) *u* wind (m s^{-1}), and (e) *v* wind (m s^{-1}); and radiosonde (f) temperature (K), (g) *u* wind (m s^{-1}), (h) *v* wind (m s^{-1}), and (i) specific humidity (g kg^{-1}),.

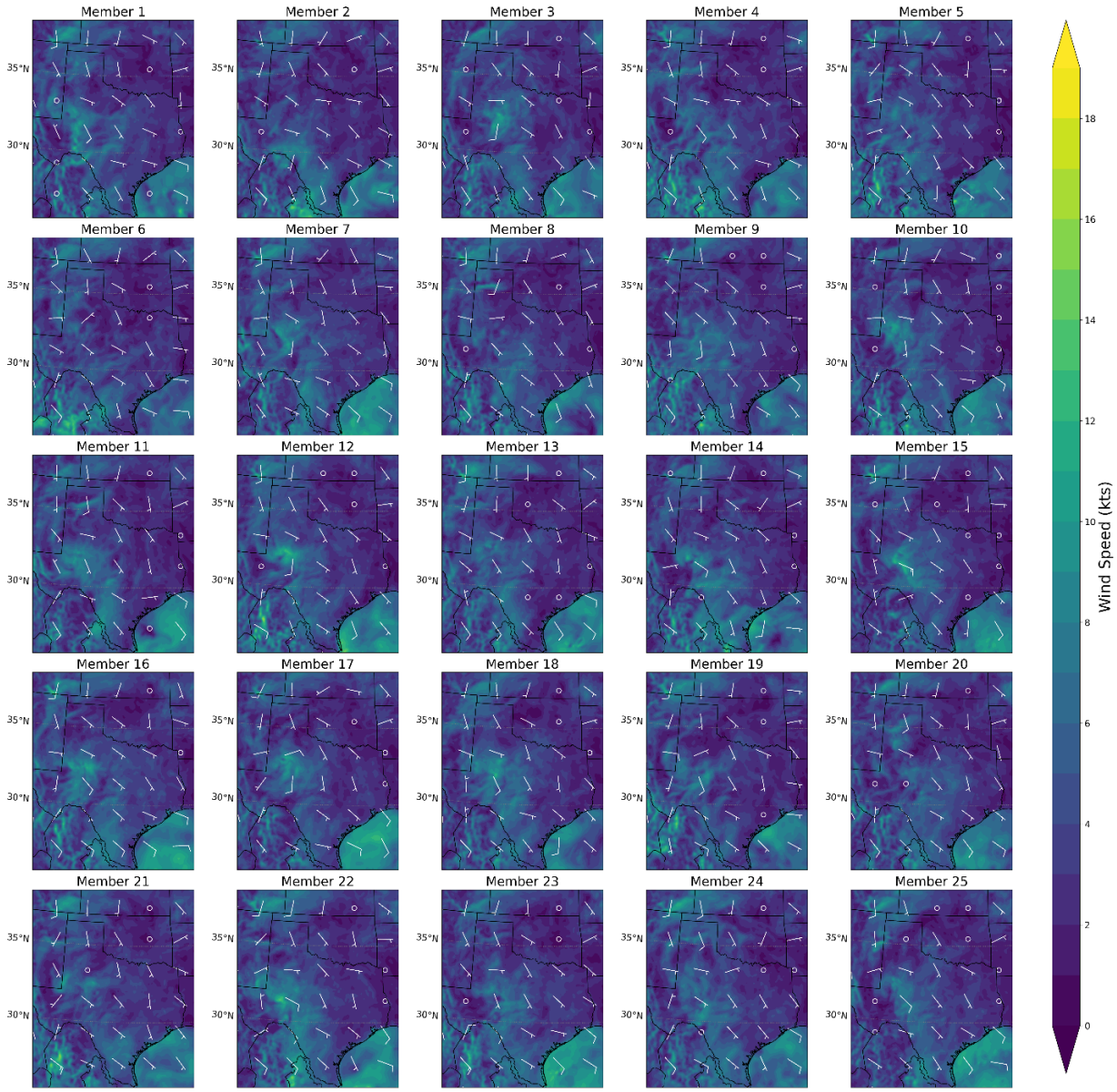

Fig. 13: Subplots of 10-m wind speed (color shaded; kts for ensemble members 1-25 at 0600 UTC 18 August 2009

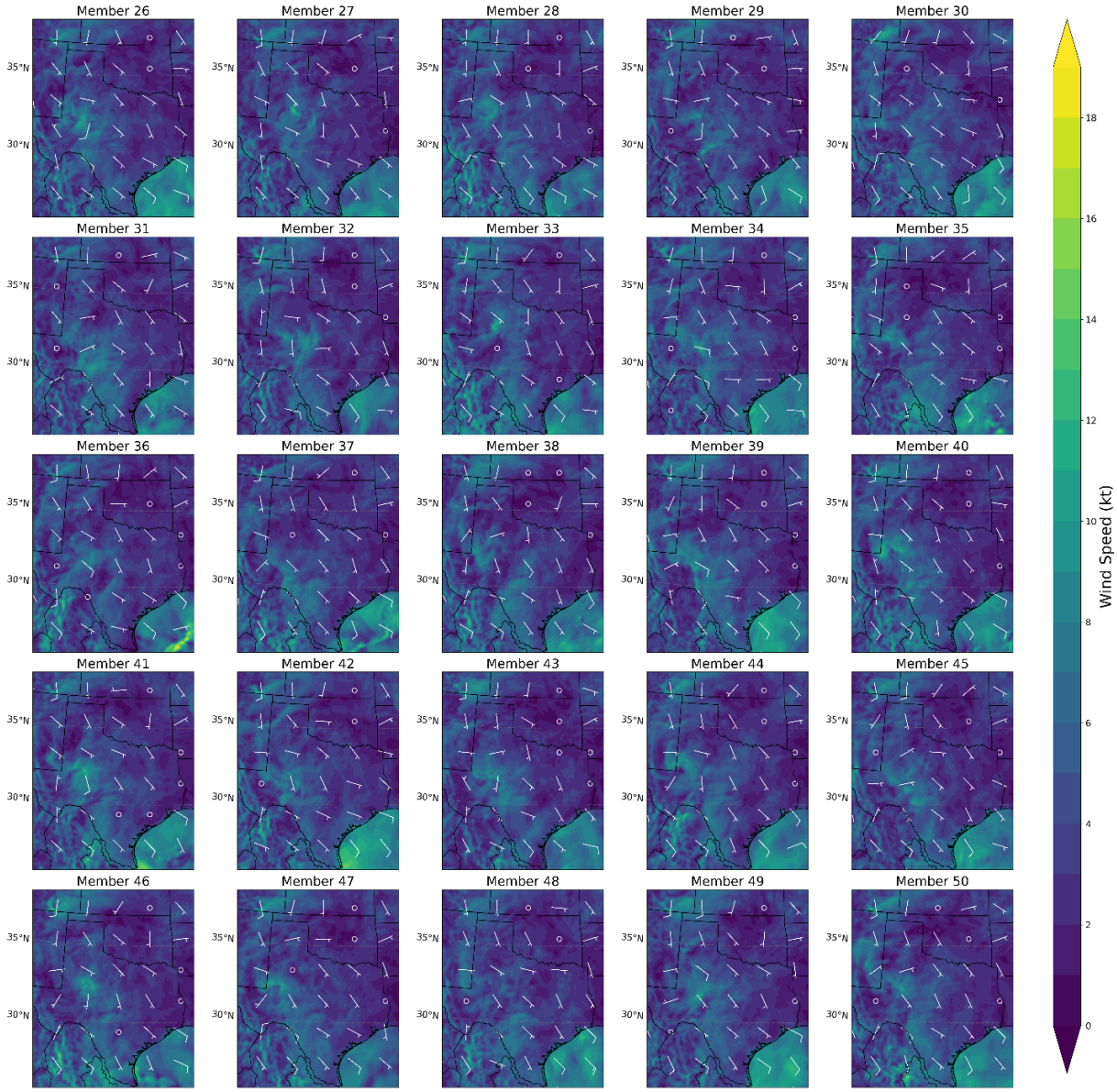

Fig. 14: Subplots of 10-m wind speed (color shaded; kts) for ensemble members 26-50 at 0600 UTC 18 August 2009

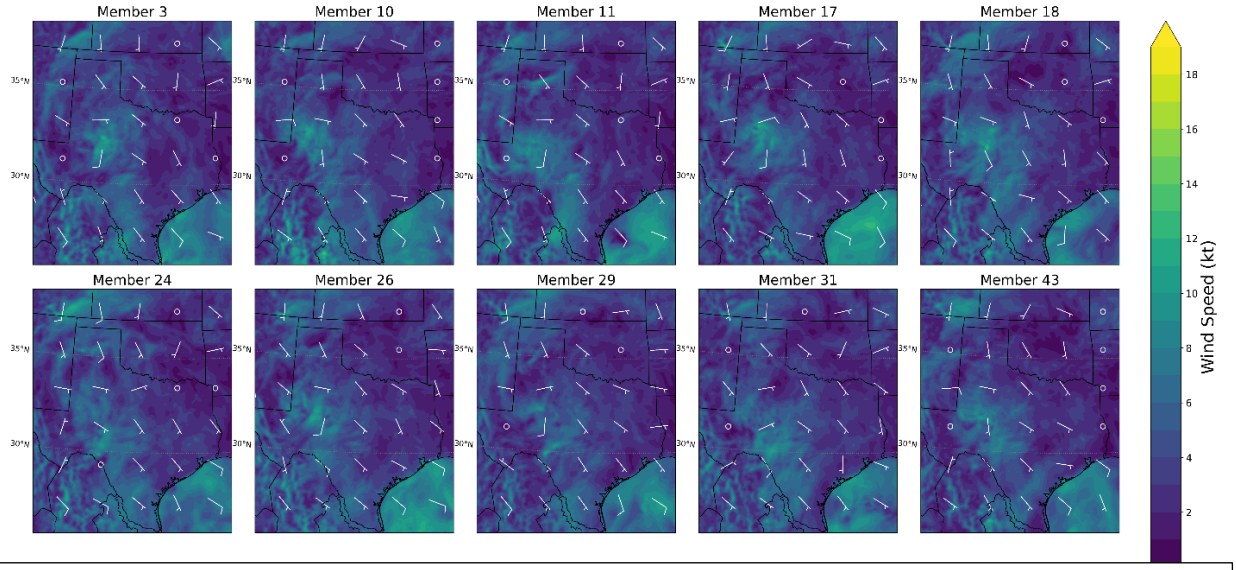

Fig. 15: Subplots of 10-m wind speed (color shaded; kts) for the chosen "GOOD" ensemble members at 0600 UTC 18 August 2009

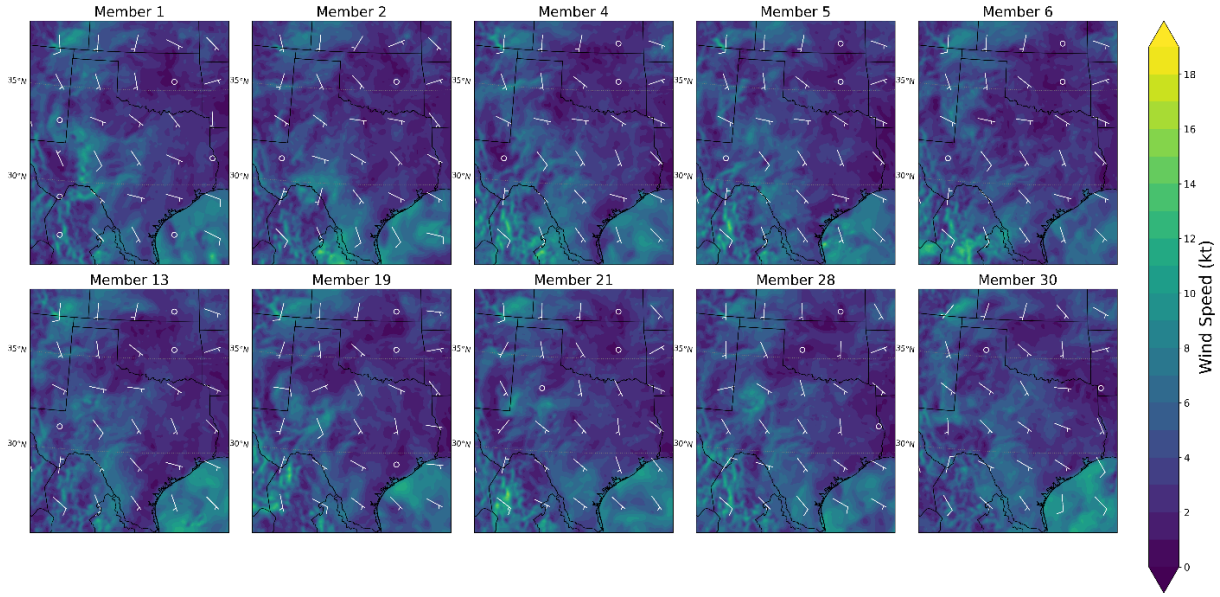

Fig. 16: Subplots of 10-m wind speed (color shaded; kts) for the chosen "BAD" ensemble members at 0600 UTC 18 August 2009

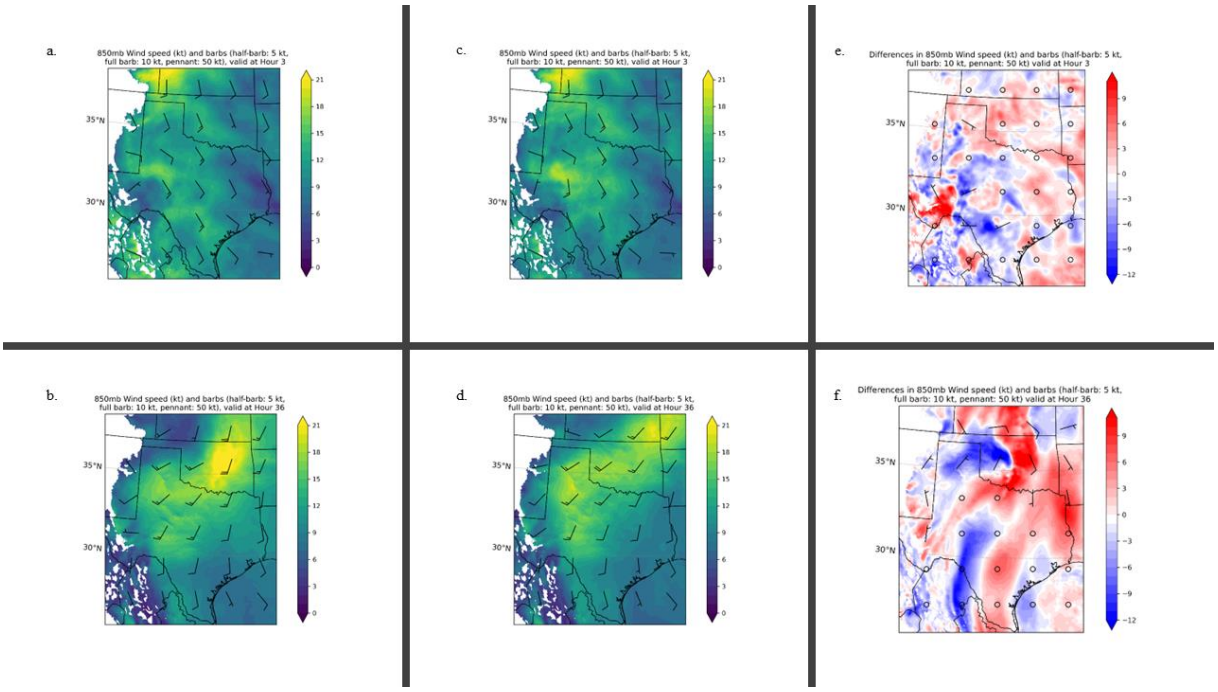

Fig. 17: 850-hPa total wind (color shaded in kt per color bar; barbs with half barb: 5 kt, full barb: 10 kt, pennant: 50 kt) at 0300 18 August 2007 for (a) GOOD, (c) BAD, and (e) GOOD-BAD; 1200 19 August 2007 for (b) GOOD, (d) BAD, and (f) GOOD - BAD

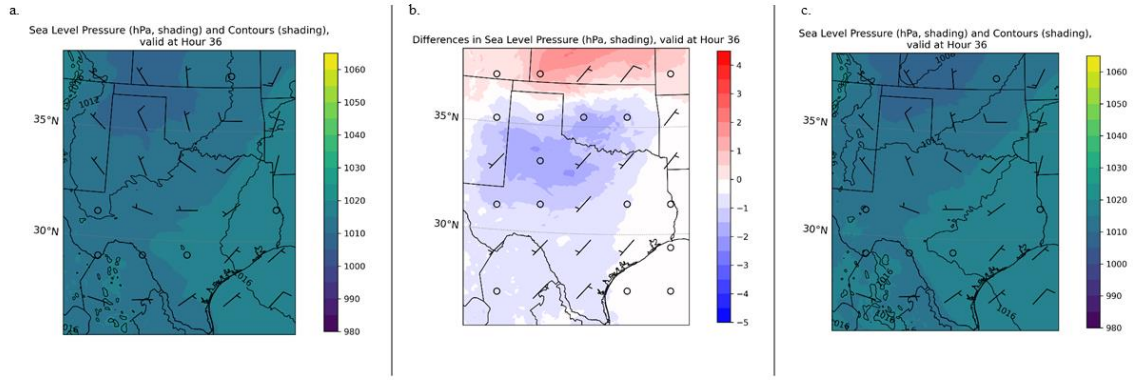

Fig. 18: 10-m wind (half barb: 5 kt, full barb: 10 kt, pennant: 50 kt) and sea level pressure (hPa, color shading) at 1200 19 August 2007 for (a) GOOD, (b) BAD, and (c) GOOD - BAD

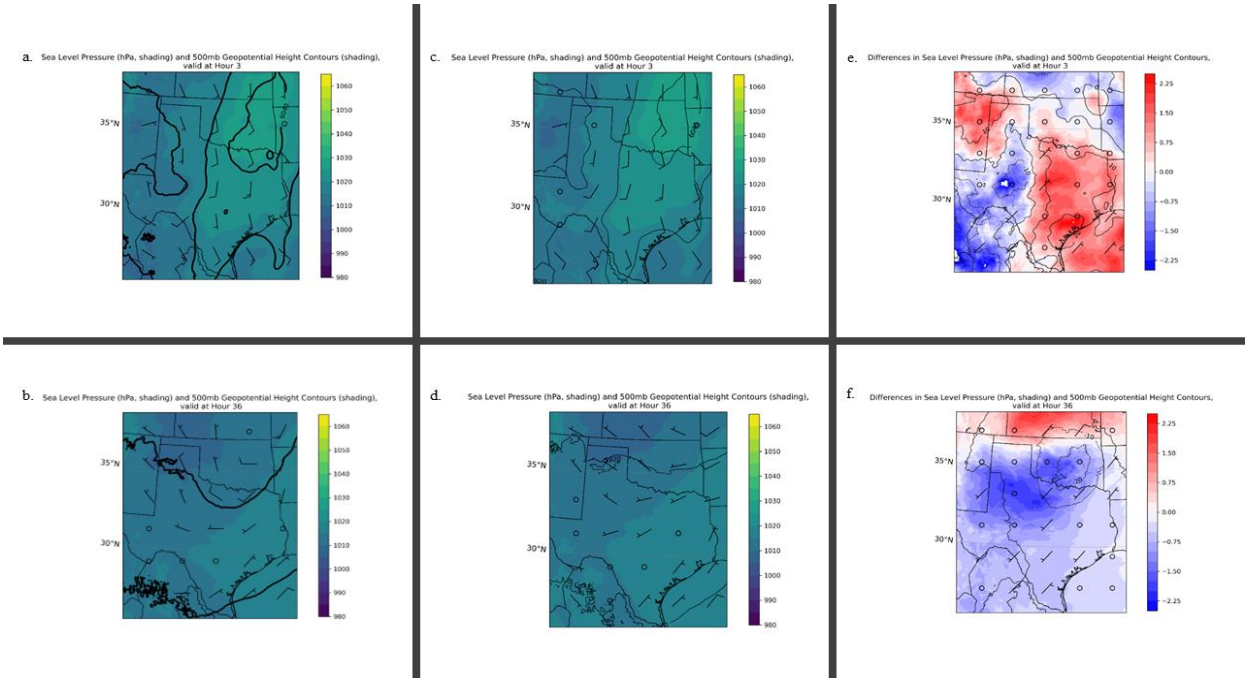

Fig. 19: 500-hPa total wind (barbs with half barb: 5 kt, full barb: 10 kt, pennant: 50 kt), 500-hPa geopotential height (m, black contours), and sea level pressure (hPa, color shaded) at 0300 18 August 2007 for (a) GOOD, (c) BAD, and (e) GOOD-BAD; 1200 19 August 2007 for (b) GOOD, (d) BAD, and (f) GOOD - BAD

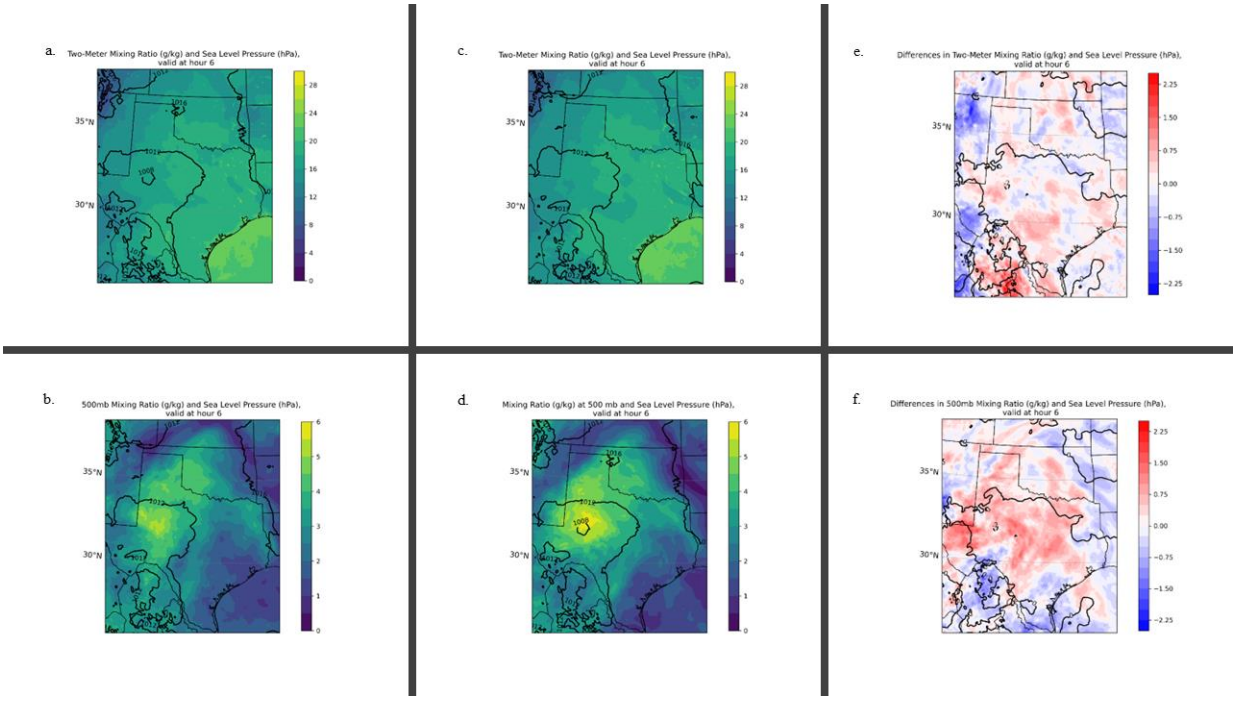

Fig. 20: 2-m and 500 hPa mixing ratio (g/kg; color shaded) and Sea Level Pressure (black contours) at 0600 18 August 2007 for (a,c) GOOD, (b,d) BAD, and (e,f) GOOD-BAD;

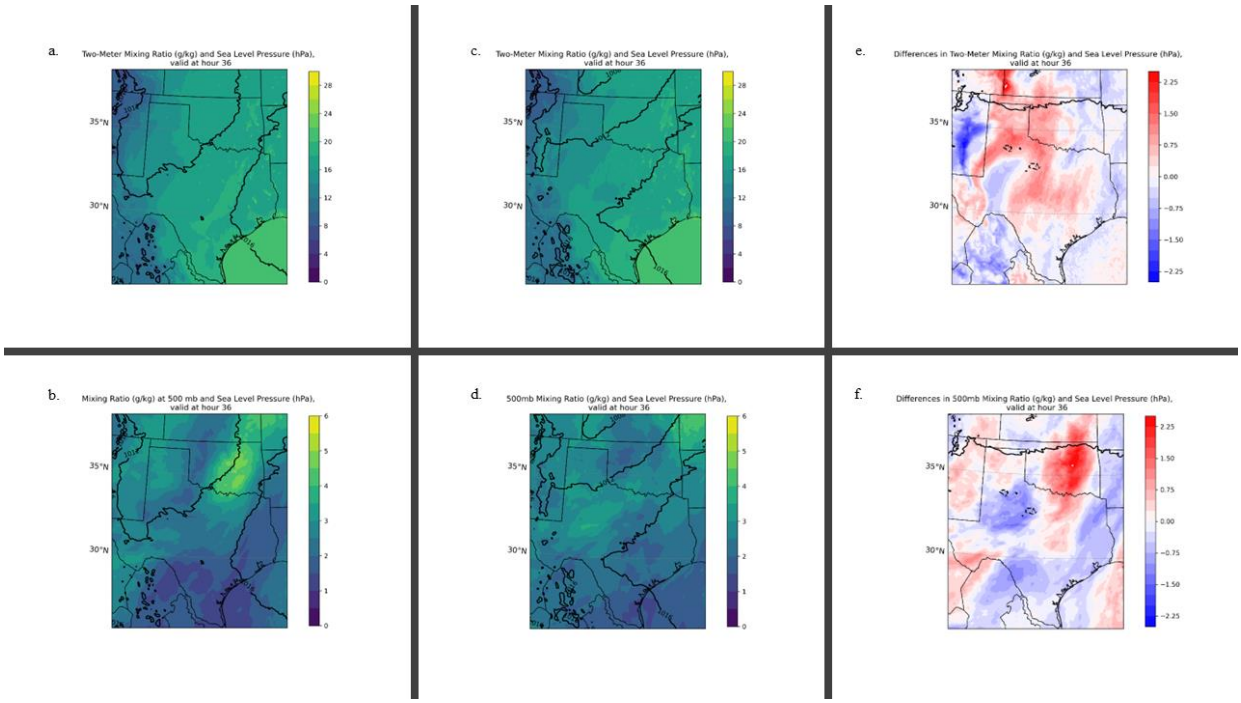

Fig. 21: Same as 20, but at 1200 UTC 19 August 2007 for (a,c) GOOD, (b,d) BAD, and (e,f) GOOD-BAD;

Appendix B: Tables

Parameter	Inner Domain	Outer/Assimilation Domain	References
Horizontal Grid	1101 x 1001 $\Delta x = 3$ km	400 x 300 $\Delta x = 15$ km	
Vertical Grid	50 levels $p_{top} = 50$ hPa	50 levels $p_{top} = 50$ hPa	
Cumulus Parameterization	None	New Tiedtke	Zhang and Wang (2017)
Boundary Layer Parameterization	Yonsei University (YSU) Planetary Boundary Layer Scheme	Yonsei University (YSU) Planetary Boundary Layer Scheme	Hong et al. (2006)
Microphysical Parameterization	Thompson Scheme	Thompson Scheme	Thompson et al. (2008)
Longwave Radiation	Rapid Radiative Transfer Model for Global Climate Models (RRTMG)	RRTMG	Iacono et al. (2008)
Shortwave Radiation	RRTMG	RRTMG	Iacono et al. (2008)
Land surface Parameterization	Noah Land Surface Model	Noah Land Surface Model	Tewari et al. (2004)

Table 1: WRF-ARW Model options for inner and outer domains.

Platform	Variable	Observation error	Observation window (h)
METAR	Temperature	Ha and Snyder (2014)	±1
	E-W, N-S winds	Ha and Snyder (2014)	±1
	Specific humidity	Schwartz et al. (2015a)	±1
	Altimeter	NCEP statistics	±1
Radiosonde	Temperature	Schwartz et al. (2015b)	±1
	E-W, N-S winds	Romine et al. (2013, 2014)	±1
	Specific humdity	Schwartz et al. (2015a)	±1
	Surface altimeter	NCEP statistics	±1
Dropsonde	Temperature	NCEP statistics	±1
	E-W, N-S winds	NCEP statistics	±1
	Specific humidity	NCEP statistics	±1
	Surface altimeter	NCEP statistics	±1
Marine	Temperature	NCEP statistics	±1
	E-W, N-S winds	NCEP statistics	±1
	Specific humidity	Schwartz et al. (2015a)	±1
	Altimeter	NCEP statistics	±1
ACARS (22.5 km, 25 hPa) [1]	Temperature	NCEP statistics	±1
	E-W, N-S winds	NCEP statistics	±1
	Specific humidity	Schwartz et al. (2015a)	±1
Profiler	E-W, N-S winds	NCEP statistics	±1
	Pressure	NCEP statistics	±1
Satellite derived (22.5 km, 25 hPa) [1]	E-W, N-S winds	Romine et al. (2013)	±1
GPS	RO refractivity	Kuo et al. (2004)	±1

[1] Superobs (horizontal, vertical)

Table 2: Assimilated observation platforms, assumed observation errors, and observation windows.